Contents lists available at ScienceDirect

Applied Catalysis B: Environmental

Enhanced photocatalytic properties of lanthanide-TiO$_2$ nanotubes: An experimental and theoretical study

Paweł Mazierski[a], Wojciech Lisowski[b], Tomasz Grzyb[c], Michał Jerzy Winiarski[d], Tomasz Klimczuk[d], Alicja Mikołajczyk[e], Jakub Flisikowski[a], Adam Hirsch[a], Agnieszka Kołakowska[a], Tomasz Puzyn[e], Adriana Zaleska-Medynska[a], Joanna Nadolna[a,*]

[a] Department of Environmental Technology, University of Gdansk, 80-308 Gdansk, Poland
[b] Institute of Physical Chemistry, Polish Academy of Sciences, Kasprzaka 44/52, 01-224 Warsaw, Poland
[c] Department of Rare Earths, Adam Mickiewicz University, 60-780 Poznan, Poland
[d] Department of Solid State Physics, Gdansk University of Technology, 80-233 Gdansk, Poland
[e] Laboratory of Environmental Chemometrics, University of Gdansk, 80-308 Gdansk, Poland

ARTICLE INFO

ABSTRACT

A series of Er-, Yb-, Ho-, Tb-, Gd-, Pr-TiO$_2$ nanotubes (RE-NTs) was prepared *via* an electrochemical method. The as-prepared photocatalysts were characterized by X-ray diffraction (XRD), X-ray photo-electron spectroscopy (XPS), UV–vis absorption, scanning electron microscopy (SEM) and luminescent spectroscopy. The experiments demonstrated that toluene in the gas phase was successfully degraded under visible light (LEDs λ_{max} = 465 nm) using RE-NTs. In the presence of the most active sample (Ho-NTs), the photodegradation of toluene reached 30% after 60 min of vis irradiation. To investigate the localization of RE in the TiO$_2$ structure, computer simulations were performed using the plane-wave-based Vienna *ab-initio* simulation package (VASP) implementing spin-polarized density-functional theory (DFT) and the generalized gradient approximation (GGA). It is proposed that during the electrochemical process, TiO$_2$ systems with new Ho-f states below the conduction band of TiO$_2$ is formed. The photocatalytic activity under Vis irradiation is attributable not to $^\bullet$OH but to other forms of reactive oxygen species ($O_2^{\bullet-}$, $HO_2^\bullet$, H_2O_2).

1. Introduction

Over the past few decades, an environmentally friendly photocatalytic process in the presence of TiO$_2$ as a photocatalyst has been utilized in various environmental applications. Among these applications, air [1], water [2] and wastewater treatments [3]; inactivation of microorganisms, such as bacteria and viruses [4]; hydrogen production by water splitting [5]; dye-sensitized solar cells [6]; and CO$_2$ conversion into useful hydrocarbons [7] are the most investigated. In many of these applications, TiO$_2$ materials are applied in the form of various morphologies, such as zero-dimensional (nanoparticles), one-dimensional (wires, rods and tubes), two-dimensional (layers and sheets) and three-dimensional

structures (spheres) [8]. One-dimensional nanostructures, in particular TiO$_2$ nanotubes (NTs), have gained increasing scientific interest because of the successful combination of their unusual physical properties with a well controllable nanotubular structure [9]. In particular, their electronic properties, including a high electron mobility or quantum confinement effects, low dimensionality and high surface-to-volume ratio, are of great interest. As a consequence, the activity/reactivity of these structures significantly increases. Considering their unique properties, NTs can be used as photocatalytic materials; however, their photoactivity is restricted to the ultraviolet light region because of a large band gap (3.2 eV), which represents only 4% of the total solar energy.

Among various strategies of modifying TiO$_2$ for the utilization of visible light, including metal [2] and nonmetal ion doping [10], codoping [11], noble metal deposition [12], and sensitization by inorganic complexes or organic dyes [13], doping with rare earth (RE) elements is a promising approach to overcome the above men-
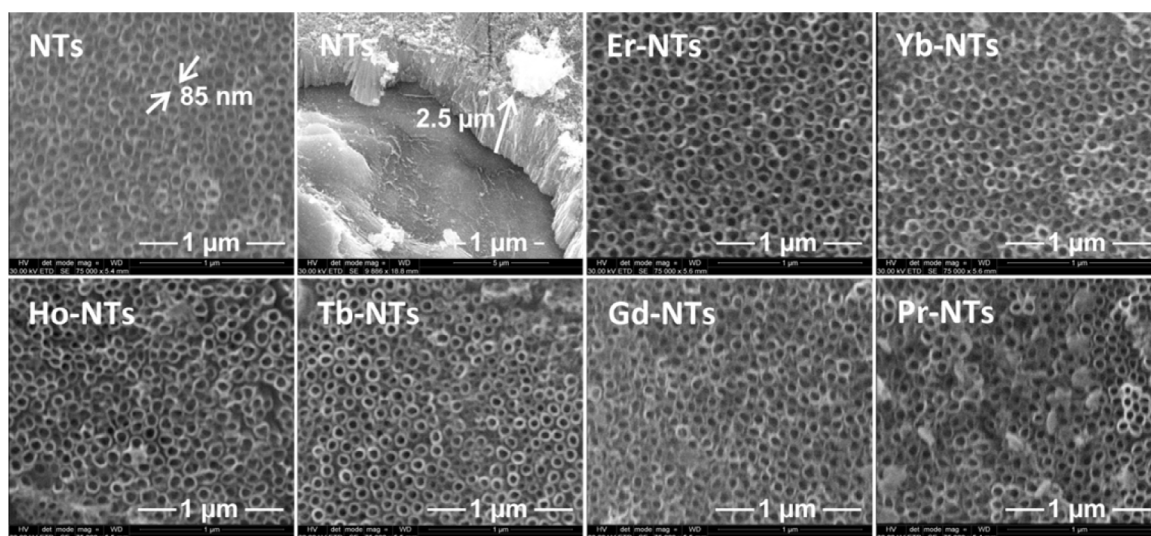
Fig. 1. Surface and cross-sectional morphologies of lanthanide-TiO$_2$ NTs.

tioned drawbacks. Additionally, it has been reported that loading RE elements into TiO$_2$ photocatalysts can alter the surface adsorption properties and the complexation of organic contaminants through the RE f-orbitals to lead to an effective outcome for environmental remediation. Furthermore, modification with RE^{3+} ions prevents the electron–hole recombination process [14] Some literature data suggested that up-conversion process can be responsible for photocatalytic activity of rare earth metals – TiO$_2$ systems under Vis lights irradiation [15] but in our previews studies, according to action spectra analysis, we failed to detect impact of up-conversion process on RE-TiO$_2$ photoactivity [14,16,17].

In the literature, the most often presented preparation routes of RE-TiO$_2$ photocatalysts have been sol-gel [18–20], hydrothermal [21] and solvothermal [22] methods, which allow one to obtain a photocatalyst in powder form. The drawback of powdered photocatalysts is the problem of separating the photocatalyst after the photocatalytic process, which hinders industrial applications of TiO$_2$. In contrast to the other methods, the electrochemical anodization approach provides a dense and well-defined layer, where NTs are perpendicularly aligned to the substrate surface. Moreover, the growth of well-defined NTs with controllable lengths is achieved in a very short time. Therefore, NTs meet the previously mentioned requirement since they can be directly grown on a support material while maintaining a high surface area, guaranteeing enhanced photon absorption together with the extensive adsorption of reactant molecules on the photocatalyst surface [23]. Consequently, RE-TiO$_2$ nanotube (RE-NT) systems may lead to successful applications in photocatalysis, as was noted by Li et al. [24].

On the other hand, the method of RE–NT preparation may have an influence on not only photocatalytic but also luminescence properties. Generally, RE-NTs are prepared by one-and two-step synthesis processes. Nie et al. [25] prepared lanthanum-doped TiO$_2$ NTs by a two-step electrochemical approach, namely, amorphous TiO$_2$ NTs were obtained in the first step followed by lanthanum incorporation into NTs in the second step by a cathodic electrochemical process using a lanthanum nitrate solution as the La source. They investigated the photoelectrochemical properties of a La-NT electrode. By contrast, Li et al. [24] obtained erbium-doped TiO$_2$ NTs via the anodization of titanium in an electrolyte containing ammonium fluoride, ethylene glycol and an erbium precursor. They showed that the photocatalytic degradation rate of methylene blue was dependent on the amount of erbium dopant. Moreover, Ce-NTs were prepared in an ethylene glycerol-based electrolyte containing

ammonium fluoride and cerium nitrate for photocatalytic hydrogen production [26].

Considering the points in the above discussion, complementary experimental and theoretical studies focusing on the above mentioned aspects have not been found in the literature. In this work, for the first time, we aimed at focusing on the synergic experimental and theoretical characterization of RE-NTs (RE = Er, Yb, Ho, Tb, Gd, Pr) prepared by a two-step electrochemical method. RE-NTs were characterized by X-ray diffraction (XRD), X-ray photoelectron spectroscopy (XPS), UV–vis absorption, scanning electron microscopy (SEM) and luminescent spectroscopy. For the first time, the photocatalytic activity of the as-prepared photocatalysts was evaluated in two model reactions (toluene degradation in the gas phase and phenol degradation in the liquid phase). To provide insight into the oxidative species participating in the degradation mechanism, a hydroxyl radical test with terephthalic acid was also studied. A possible mechanism for the generation of a reactive oxygen species under visible light irradiation was proposed as well. Calculations were performed using the plane-wave- based Vienna *ab-initio* simulation package (VASP) implementing spin-polarized density functional theory (DFT) and generalized gradient approximation (GGA).

2. Experimental section

2.1. Materials

A titanium foil (0.127 mm thickness, 99.7% purity, Sigma Aldrich, Poland) was cut into pieces of 30 × 20 mm. Isopropanol, acetone, methanol, ethylene glycol, ammonium fluoride, phenol, terephthalic acid and toluene were purchased from POCh S.A, Poland. Rare earth nitrates and anhydrous CuSO$_4$ were purchased from Sigma-Aldrich, Poland. All aqueous solutions were prepared using deionized (DI) water with a conductivity of 0.05 μS.

2.2. Preparation of RE^{3+}-TiO$_2$ NTs

Pristine TiO$_2$ NTs were prepared by using a one-step anodization process. First, the titanium foils were ultrasonically cleaned in acetone, isopropanol, methanol and deionized water (10 min for each solvent) and dried in an air stream. These foils were anodized for 60 min with a constant voltage of 30 V in an electrolyte composed of 0.1 M NH$_4$F, 2 vol% water and 98 vol% ethylene glycol. Anodiza-
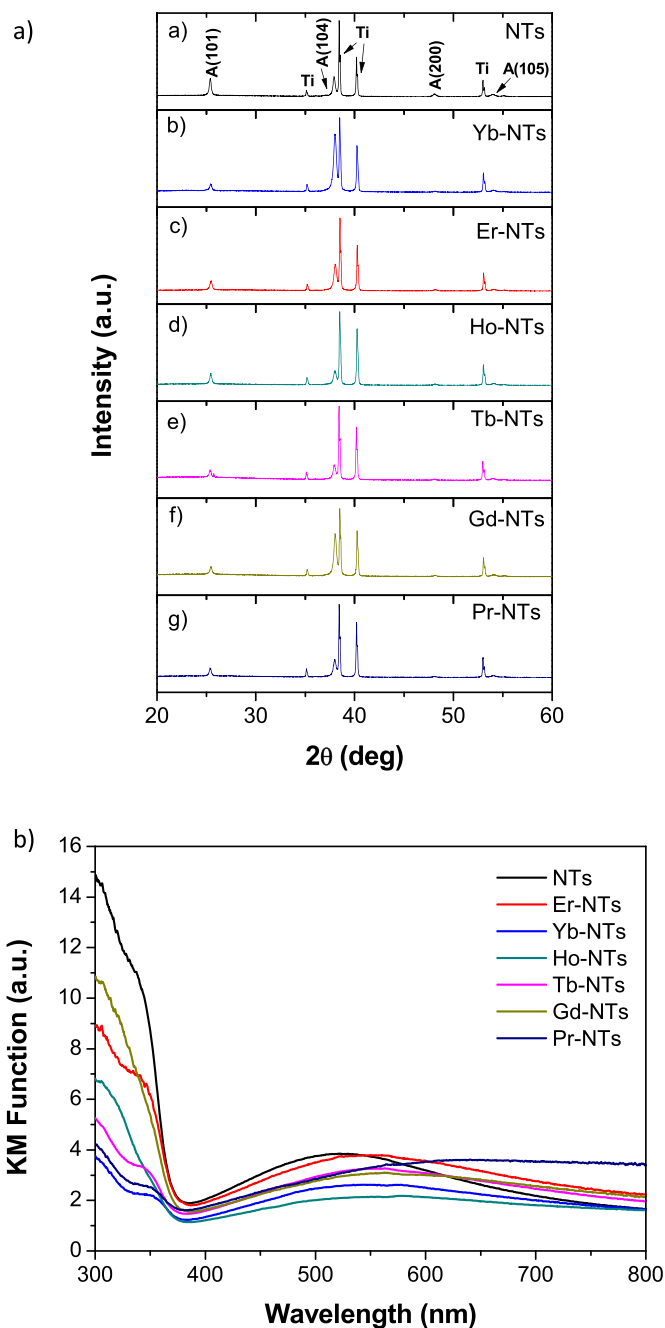
a)

Fig. 2. a) X-ray diffraction patterns of pristine TiO_2 NTs (a) and lanthanides − TiO_2 NTs (b-g). Vertical bars represent the expected Bragg positons for TiO_2 (anatase). b) UV–vis Kubelka-Munk absorption of RE^{3+}-TiO_2 NTs.

tion was performed at room temperature using a two-electrode system with Ti foil as the anode and platinum mesh as the cathode. After anodization, the amorphous TiO_2 NTs were rinsed with deionized water, sonicated in water (5 min) and dried in an air stream. Lanthanide- TiO_2 NTs were prepared by using a cathodic electrochemical process. The amorphous TiO_2 NTs were used as the cathode, and the platinum mesh was used as the anode. The electrolytes were 0.025 M $RE(NO_3)_3$ aqueous solutions (RE: Gd, Ho, Er, Yb, Tb and Pr). Electrochemical doping was conducted at 2 V for 30 min. After electrochemical doping, the obtained samples were rinsed with deionized water, dried in air (80 °C for 24 h) and calcinated at 450 °C (heating rate 2 °C/min) for 1 h.

2.3. Characterization of RE^{3+}-TiO_2 NTs

The morphology of the obtained samples was determined by using scanning electron microscopy (SEM, FEI Quanta 250 FEG). The UV–vis reflectance and absorbance spectra of pristine and lanthanide-TiO_2 NTs were recorded on a Shimadzu UV–vis spectrophotometer (UV 2600) equipped with an integrating sphere. The sample's composition was checked by X-ray diffraction using an X'Pert Pro MPD Philips diffractometer with Cu Kα radiation ($\lambda = 1.5418\,\text{Å}$). Measurements were performed in a 2θ range of 20–80°. Emission spectra were measured with the use of a QuantaMaster^{TM} 40 (Photon Technology International) spectrophotometer equipped with an Opolette 355LD UVDM (Opotek Incorporation) tuneable laser (excitation source) with a repetition rate of 20 Hz and a Hamamatsu R928 photomultiplier as the detector. X-ray photoelectron spectroscopy measurements were performed using a PHI 5000 VersaProbe (ULVAC-PHI) spectrometer with monochromatic Al Kα radiation (hν = 1486.6 eV) from an X-ray source operating at 25 W and 15 kV and a 100 μm spot size. High-resolution (HR) XPS spectra were collected with a hemispherical analyser at a pass energy of 23.5 eV, an energy step size of 0.1 eV and a photoelectron take-off angle of 45° with respect to the surface plane. CasaXPS software (version 2.3.16) was used to evaluate the XPS data. The binding energy (BE) scale of all detected spectra was referenced by setting the BE of the aliphatic carbon peak (C−C) signal to 285.0 eV.

2.4. Theoretical calculations

Calculations were performed using the plane-wave-based Vienna *ab-initio* simulation package (VASP) [27–29], implementing spin-polarized density functional theory (DFT) and the generalized gradient approximation (GGA) by Perdew-Burke-Ernzerhof (PBE) with intra-site Coulomb interactions between Ti-3d electrons in Dudarev's approach; here, we call the method, PBE + *U*. The core electrons for Ho-(Xe)4f^{11}, O-1s^2 and Ti-(Ne)3s^2 were described by the projector augmented wave potential (PAW) [30–32]. Using a cut–off energy of 400 eV and a Γ-centred Monkhorst-Pack grid with a 0.03 Å^{-1} separation (equivalent to a *k*-point mesh of $8 \times 8 \times 11$, $3 \times 7 \times 1$ and $2 \times 2 \times 1$ for bulk anatase, TiO_2(101)-(1 × 1)), the total energy was forced to converge to <1 meV/atom. All of the structures considered in this study were fully relaxed until all of the forces were <0.02 eV Å [27]. In this study, we used a *U* value of 3.5 eV, which has been found to be suitable as a proper description of the anatase crystal compared with experiments [33,34]. The PBE + *U*-computed optimal lattice parameters for bulk anatase TiO_2 were $a = b = 3.85\,\text{Å}$, $c = 9.72\,\text{Å}$ [35]. The anatase TiO_2(101) surface was modelled with three O-Ti-O layers (Fig. 6a) along the (001) direction and a 15 Å vacuum thickness between the slabs. All of the atoms in the system were allowed to relax, except for the bottom O-Ti-O layer, which was kept fixed to mimic the bulk structure. In this work we also studied the doping of a Ho atom on a reduced TiO_2(101) surface. To model the reduced TiO_2(101) surface, we created a surface oxygen vacancy (V_O^{sur}) and a subsurface vacancy (V_O^{sub}) by removing one bridging oxygen or titanium atom from the system, as depicted in Fig. 6. In conclusion, for the sake of comparison, 144-atom supercells were used to construct all of the calculation models. In addition, one oxygen/titanium atom in the supercell was replaced by a holmium atom to generate a Ho-TiO_2 system.

2.5. Photocatalytic experiments

The photocatalytic properties of the obtained RE-NTs were determined by a three model process: purification of air from
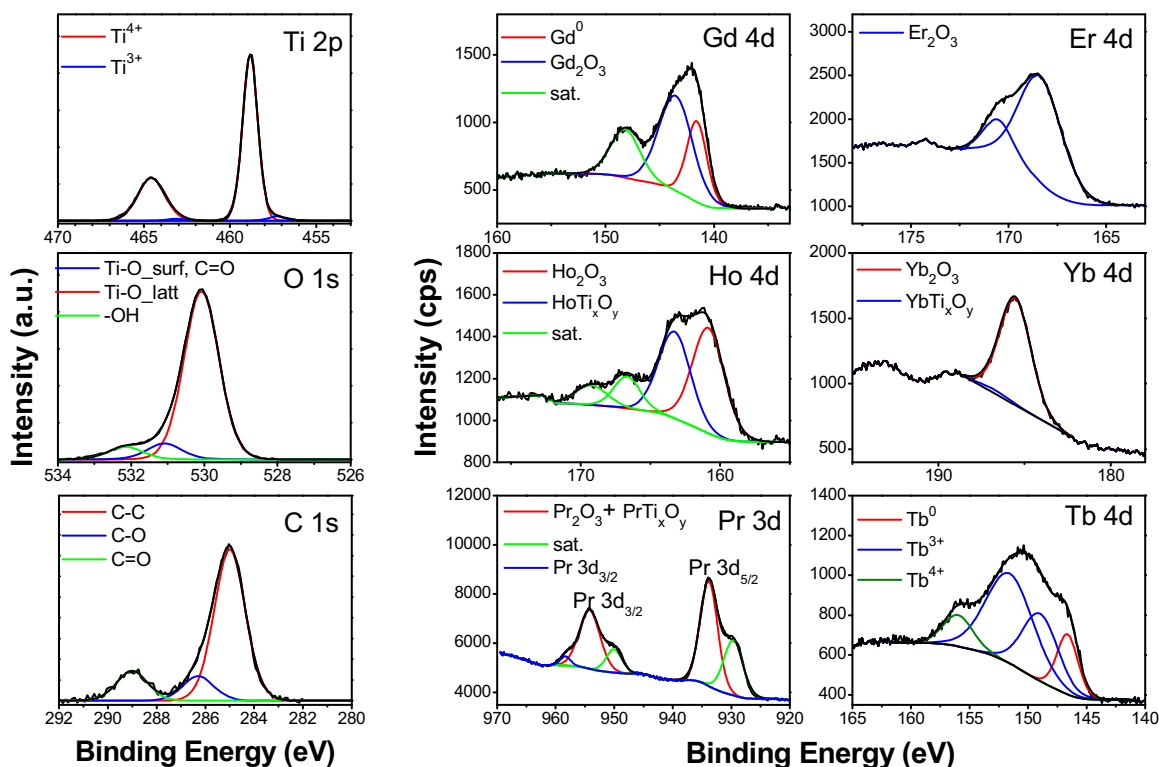
Fig. 3. XPS spectra of as-prepared RE-TiO$_2$ NTs.

toluene, treatment of water from phenol and $^{\bullet}$OH radical generation efficiency (using terephthalic acid) under visible light irradiation. The experimental procedures have been described in our previous papers [2,23,36]. Terephthalic acid reacts with hydroxyl radicals forming highly fluorescent product: 2-hydroxyterephthalicacid. Photocatalytic activity tests in the water phase (phenol degradation and $^{\bullet}$OH radical generation) were carried out in a photoreactor made of quartz with a working volume of approximately 10 mL, while air purification tests were performed using an array of 25 Vis LEDs (λ_{max} = 465 nm) as an irradiation source. Toluene degradation in the gas phase was carried out in a flat stainless steel photoreactor with the working volume of about 35 mL. Reference toluene, phenol and terephthalic acid samples (200 μL, 0.5 mL and 0.5 mL, respectively) were taken just before starting the irradiation, and subsequent samples were collected at regular time periods (10, 20 and 20 min, respectively) during irradiation. The RE-NT samples with the surface area of 4 cm^2 were immersed in phenol (C$_0$ = 0.21 mM) or terephthalic acid solution (C$_0$ = 0.5 mM) for 30 min in the dark to achieve adsorption-desorption equilibrium. Aqueous solution containing model compound was continuously stirred (500 rpm) and irradiated using a 1000 W Xenon lamp (Oriel 66021).

The analysis of toluene concentration in the gas phase was performed using gas chromatograph (Trace 1300, Thermo Scientific) equipped with flame ionization detector (FID) and Elite-5 capillary column. The samples (200 μL) were dosed by using a gas-tight syringe. Phenol concentration was estimated by the colorimetric method after derivatization with p-nitroaniline using UV–vis spectrophotometer (λ_{max} = 480 nm). Fluorescence spectra (detection of $^{\bullet}$OH radical) were recorded at room temperature by using a LS–50 B Luminescence Spectrophotometer equipped with Xenon discharge lamp as an excitation source (excitation wavelength 315 nm) and a R928 photomultiplier detector. Irradiation intensity was measured by an optical power meter (HAMAMATSU, C9536-01) and equal to

4 mW/cm^2 (aqueous phase) and 0.25 mW/cm^2 (gas phase) for Vis irradiation.

To investigate the role of the excess electrons in the photocatalytic process, the photocatalytic activity test in the water phase was conducted in the presence of Cu^{2+} scavenger. In this case, CuSO$_4$ water solution (C = 2.5 × 10^{-3} M) was added to the reactor together with phenol aqueous solution.

3. Results and discussion

3.1. Surface morphology of RE-NTs

Fig. 1 shows the surface and cross-sectional morphologies of the obtained pristine and lanthanide- TiO$_2$ NTs. As observed in the SEM images, all of the samples were uniform and highly ordered over all of the observed area. The tops of the pristine and lanthanide-NTs were open, without any impurities. In addition, oxide ripples on the outer walls of the NTs were not observed. Notably, electrochemical modification of the NTs with lanthanides did not influence the dimensions of the RE-NTs. It is likely that only the presence of RE atoms could affect the photocatalytic properties because the morphology of the NTs after RE incorporation was not changed. All of the obtained samples had the same dimensions, namely, the outer diameter, wall thickness and tube length were equal to 85 ± 3, 15 ± 0.5 nm and 2.5 ± 0.06 μm, respectively. The developed surface area and porosity were calculated based on [37,38], and all of the samples' values were equal to 617 ± 5 cm^2 and 0.70 ± 0.1, respectively.

3.2. Crystal structure of RE-NTs

The X-ray diffraction patterns of pristine (a) and lanthanide-TiO$_2$ NTs (b–g) are shown in Fig. 2. Two phases were detected: Ti metal and TiO$_2$ in the form of anatase. The sharp and intense reflections come from Ti foil, whereas the broad and low intensity

Table 1
Sample labels, characterization and photocatalytic activity of lanthanide- TiO$_2$ NTs (r – initial reaction rate; k – reaction rate constant; RE^{3+} radii – literature data).

Sample lable	dopant type	RE^{3+} radii (pm)	Crystallite size (nm)	Cell parameters (Å)		Cell volume, V (Å^3)	XPS analysis						Toluene photodegradation (Vis irradiation λ=465 nm)	
				a = b	c		Ti (at.%)	Ti^{4+} (%)	Ti^{3+} (%)	O (at.%)	C (at.%)	RE^{3+} (at%)	r (μmol min^{-1})	k (min^{-1})
NTs	none	none	38	3.7904 ± 0.0002	9.5107 ± 0.0004	136.64 ± 0.02	25.2	95.3	4.7	60.2	14.6	none	0.0002	0.0007
Er–NTs	Er	89	36	3.7923 ± 0.0003	9.5021 ± 0.0003	136.65 ± 0.03	18.7	98.1	1.9	63.3	13.3	4.7	0.0028	0.0043
Yb–NTs	Yb	86.8	35	3.7962 ± 0.0004	9.5030 ± 0.0003	136.95 ± 0.03	21.2	95.9	4.1	61.6	15.1	2.1	0.0005	0.0036
Ho–NTs	Ho	90.1	36	3.7929 ± 0.0003	9.5044 ± 0.0005	136.73 ± 0.03	21.7	93.8	6.2	62.0	13.2	3.1	0.0025	0.0060
Tb–NTs	Tb	92.3	34	3.7918 ± 0.0004	9.5011 ± 0.0005	136.60 ± 0.04	21.4	95.3	4.7	58.9	14.6	5.0	0.0038	0.0058
Gd–NTs	Gd	93.8	35	3.7943 ± 0.0003	9.5017 ± 0.0003	136.79 ± 0.03	22.8	95.5	4.5	60.9	11.7	4.6	0.0017	0.0057
Pr–NTs	Pr	99	34	3.7925 ± 0.0003	9.4948 ± 0.0004	136.56 ± 0.03	22.2	95.6	4.4	62.1	9.5	6.2	0.0009	0.0044

originated from the anatase phase. The diffraction peaks at 25.39°, 37.95°, 47.81° and 53.19° can be ascribed to (101), (004), (200) and (105) crystallographic planes of TiO$_2$ anatase while the other ones can be described to Ti substrate (JCPDS database). The TiO$_2$ lattice parameters were estimated by the LeBail method using the Full-Prof package [39], and the average crystallite size was calculated using the Scherrer equation. The values are gathered in Table 1. The anatase lattice parameters did not change after RE^{3+} doping, and the unit cell volume were approximately 136.64 ± 0.02 and 136.95 ± 0.03 Å^3 for pristine TiO$_2$ NTs and Yb-NTs, respectively. In this case, a possible influence of the ionic radii of the lanthanides on the unit cell volume might be considered. The ionic radii of rare earth metal dopants are listed in Table 1, and they are almost 50% larger than those of Ti^{4+} (61 pm) [16]. Lack of the expansion of the TiO$_2$ cell volume after lanthanide modification, suggests that RE^{3+} species are located at the crystal boundaries rather than inside TiO$_2$ unit cell. Consequently, it is very likely that the surrounding rare earth ions formed Ti—O—RE element bonds at the crystal boundary of TiO$_2$ [40]. The crystallite size varies from 34 nm to 38 nm, the latest estimated for unmodified TiO$_2$ NTs. It is likely that Ti—O—RE element bonds inhibit phase transformation from anatase to rutile and crystallite growth by restricting direct contact between crystallites [14,40,41].

3.3. Chemical composition of RE-NTs

Table 1 shows the atomic composition of the elements detected in the surface layer of pristine and lanthanide- TiO$_2$ NTs. The surface compositions of Ti, O, C, Ga, Ho, Pr, Er, Yb and Tb were evaluated using high-resolution (HR) Ti 2p, O 1s, C 1s, Gd 4d, Ho 4d, Pr 3d, Er 4d, Yb 4d and Tb 4d XPS spectra, respectively. The relative contribution of two Ti components, assigned to Ti^{4+} and Ti^{3+}, is also presented in Table 1. An inspection of these data clearly shows that Ti^{4+} (459 eV) was the dominant surface state. The largest contribution of the Ti^{3+} (458 eV) species was found in Ho-NTs, and the lowest contribution in the Er-NTs sample. The chemical character of the elements originating from pristine TiO$_2$ and the lanthanides detected within the surface layer of the lanthanide- TiO$_2$ samples were identified from the HR XPS spectra presented in Fig. 3. The Ti, O and C surface species are described in the deconvoluted XPS spectra of Ti 2p, O 1s and C 1s, which are presented in the left column, in addition to the original HR XPS spectra of the lanthanides. The last spectra confirm reveal the complex character of their surface compounds. The Gd 4d$_{5/2}$ signals at BEs of 141.6, 143.5 and 148.2 eV correspond to Gd^0, Ga$_2$O$_3$ and a satellite peak, respectively [42,43]. The Er 4d region exhibits a complex multiplet splitting [44]. The Er 4d peaks, located at BEs 168.4 and 170.5 eV, can be attributed to Er$_2$O$_3$ [16,42,43]. The main peak in the Yb 4d spectrum at BE 185.5 eV indicates Yb$_2$O$_3$ [16,42,43,45] formation, and a small peak at BE 186.5 eV can be assigned to a YbTi$_x$O$_y$ adspecies [45]. The Ho 4d spectrum reveals two states of Ho species at BEs 160.8 and 163.3 eV, which can be ascribed to Ho$_2$O$_3$ [42,43] and HoTi$_x$O$_y$ [45]. The formation of a Ho—O—Ti bond on the surface was lately found to affect the transformation of TiO$_2$ to H$_2$Ti$_3$O$_7$ compounds [46]. The shape of the Pr 3d core level spectrum agrees well with the XPS data presented in [47]. The main peaks at BEs 933.8 and 954.2 eV indicate characteristic 3d$_{5/2}$ and 3d$_{3/2}$ components of Pr$_2$O$_3$ [42,43,47]. The peaks are accompanied by satellites at BEs 929.6 and 950.0 eV, as well as a small extra peak in the 3d$_{3/2}$ component [47]. The Pr 3d$_{5/2}$ peak is slightly shifted to a higher BE compared with pristine Pr$_2$O$_3$ (933.2 eV [43]), which can suggest a small contribution from a PrTi$_x$O$_y$ surface species located at 935.3 eV [48]. The Tb 4d spectrum is well fitted by 4 peaks at BEs 146.6, 149.0, 151.6 and 156.0 eV. The first peak originates from Tb^0 [43], the next two peaks are char-
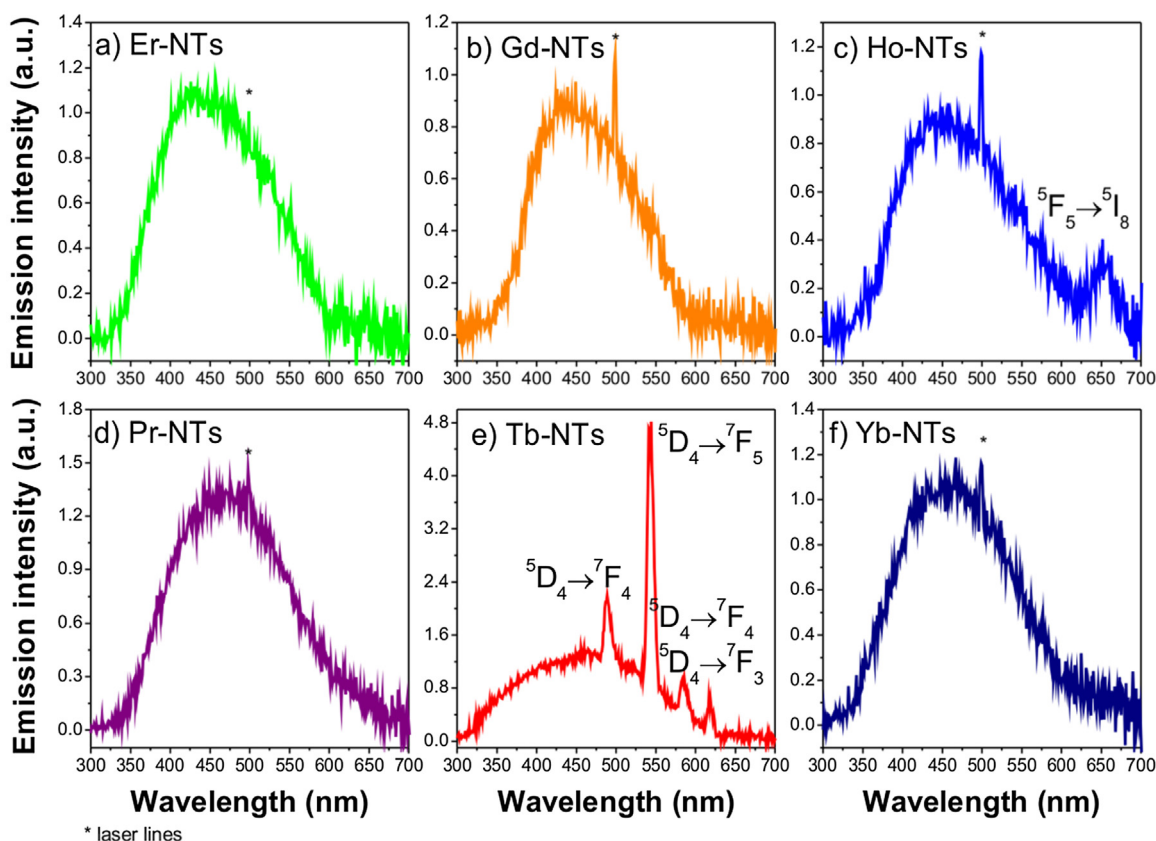
Fig. 4. Emission spectra of lanthanide- TiO$_2$ NT samples under the excitation of a laser with wavelength λ = "250 nm.

acteristic of Tb^{3+} features [49], and the last peak is characteristic of Tb^{4+} [49] compounds.

3.4. Optical and luminescence properties of RE-NTs

The results of the UV–vis DRS presented in Fig. 2b showed a broad band in the range of 400–700 nm, for all samples and is attributed to organic contaminants or is caused by trapped electrons at the Ti^{3+} centre [50]. Absorption bands in the visible region from RE^{3+} were not detected because of broad band attributed to NTs TiO$_2$. According to the KM equation (results are not shown), the pristine TiO$_2$ NTs exhibited a band gap of approximately 3.35 eV and the lanthanide- TiO$_2$ NTs values varied from 3.30 to 3.32 eV. This small difference may be due to the presence of oxygen vacancies and others surface defects [51].

The spectroscopic properties of lanthanide- TiO$_2$ NTs were analysed by measuring their emission spectra under laser excitation. The obtained NTs presented a high absorption of UV light, as presented in Fig. 2b. Therefore, laser light with λ = 250 nm was used as the excitation source, giving the highest luminescence intensity. TiO$_2$ is known from its luminescence under UV light and also by the observed emission from our TiO$_2$ materials. In all of the measured spectra presented in Fig. 4, a broad-band emission was recorded with a maximum at approximately 450 nm. The emission bands of TiO$_2$ NTs were relatively broad, ranging from 310 to 650 nm. This emission was poorly visible by the naked eye as the surface of the prepared materials was dark. In all of the studied samples, the emission intensity was similar.

The as-prepared materials were mostly in the form of their oxides. Ln^{3+} ions are known from their luminescent properties which result from f–f electronic transitions, with characteristic narrow emission bands [52]. In the studied samples, such emission

was also observed, however, only for Tb- and Ho- activated materials (see Fig. 4c and e). These two luminescence activators can be excited by UV light. Especially Tb^{3+} ions show intense luminescence under UV light [53]. This is caused by their effective absorption of light in the UV region, which is the result of allowed f-d transitions. Another factor responsible for the intense luminescence of Tb^{3+} ions is the large gap between $^5D_4$ excited and ^7F_J ground states, which decreases the probability of quenching processes. This property is also responsible for the effective luminescence of Eu^{3+} ions (not used is our studies) and causes the usually high emission quantum yields of materials doped by these two ions. Other Ln^{3+} ions have substantially more complex electronic structures and are prone to quenching processes, such as cross-relaxation, which can be enhanced when the distribution of Ln^{3+} ions is not homogenous. This explains why the emission was intense and the detection possible for only the Tb- sample. The emission spectra of Tb- TiO$_2$ presented in Fig. 4e are composed of a TiO$_2$ broad emission and four narrow bands that are characteristic of Tb^{3+} ions. In the Ho-NTs sample, the emission was weak, but detectable. The rest of the materials presented only the emission of TiO$_2$, as the remaining Ln^{3+} ions could not be excited by the excitation light used.

The obtained samples were excited also by other laser wavelengths, selected as optimal for the type of the RE ion (covering typical absorption bands of RE ion, e.g. Er^{3+}- sample was excited by laser lines with 375, 530, 650 and 980 nm). However, emission was not detected.

Emission observed in the case of Tb^{3+}- TiO$_2$ sample confirmed photoactivity of these ions and the existence of their well-defined energetic states, being in the range of TiO$_2$ band gap. From this result, it can be assumed that the 4f energy states of the remaining RE^{3+} ions were not affected by the crystal field of TiO$_2$ structure as well as impurities, quenching and decreasing participation of RE^{3+}
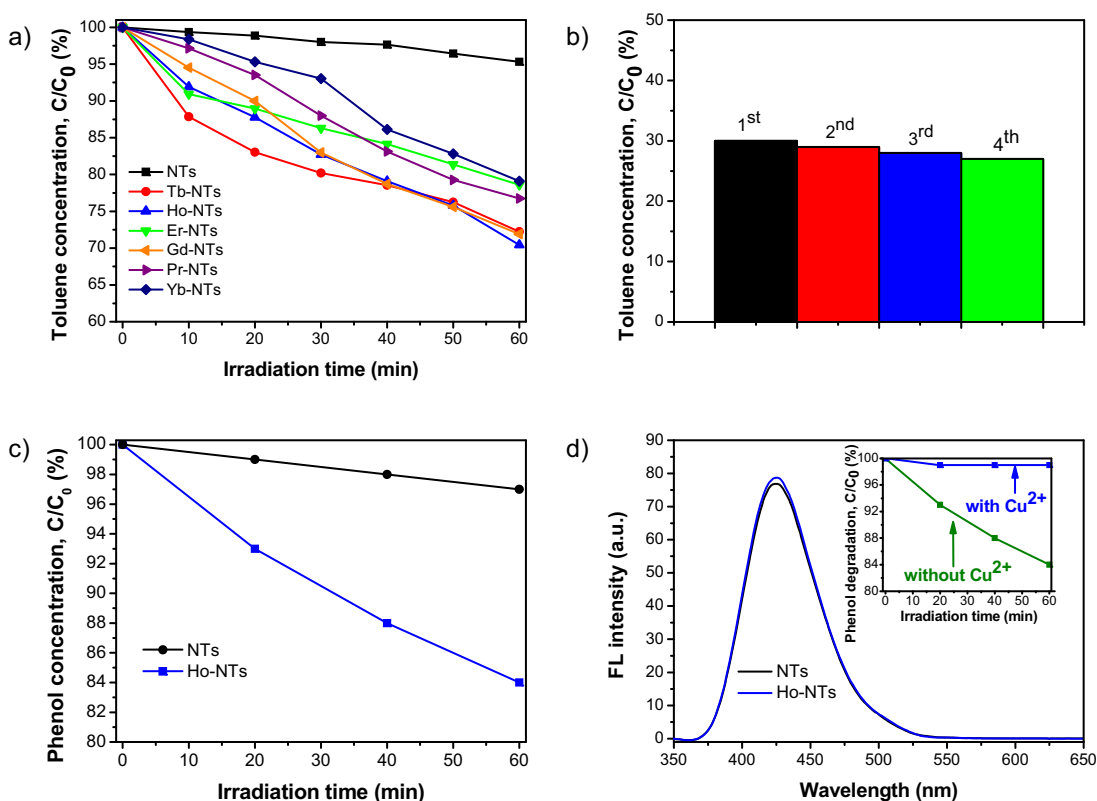
Fig. 5. Photocatalytic properties of as-prepared RE-NTs: a) efficiency of toluene degradation ($\lambda_{max} = 465$ nm), b) photostability in the toluene degradation reaction, c) degradation of phenol under vis irradiation ($\lambda > 420$ nm) and d) photoluminescence spectral changes in 5×10^{-4} M solution of terephthalic acid under vis light irradiation ($\lambda > 420$ nm); (insert graph) phenol photodegradation under different photocatalytic test conditions (with and without Cu^{2+}).

ions in photo-activated processes. Excitation into TiO_2 absorption band with resulting RE^{3+} emission confirm also energy migration between TiO_2 matrix and RE what should be also present under Vis irradiation. Recorded luminescence cannot be directly compared with photocatalytic properties as not all excitation processes may result in radiative relaxation (luminescence).

3.5. Photocatalytic properties of RE-NTs

The effect of selected lanthanides on the photocatalytic degradation of toluene over RE^{3+}-TiO_2 NTs in the gas phase under Vis irradiation (LEDs, $\lambda_{max} = 465$ nm) is presented in Fig. 5a and Table 1 (calculated as an initial reaction rate and reaction rate constant). The toluene concentration decreased in the dark experiment (without irradiation, but with the photocatalyst) by approximately 5% after 60 min (for all of the samples), while a toluene loss was not observed during direct irradiation in the absence of a photocatalyst (photolysis test). It was found that all of the lanthanide- TiO_2 NTs revealed a higher photocatalytic activity compared with the pristine one. The highest efficiency of toluene degradation (reaching approximately 30%) under Vis irradiation was observed for holmium-TiO_2 NTs, while ytterbium- and erbium-NTs exhibited the lowest photoactivities (approximately 21% and 22%, respectively). When gadolinium and terbium were used as dopants, the degradation efficiency decreased gently, reaching 28% removal after 60 min of vis irradiation. It should be noted that the most photoactive sample exhibited the highest reaction rate constant ($0.006 \, min^{-1}$) and a high (but not the highest) initial reaction rate ($0.0025 \, \mu mol \, min^{-1}$, calculated for the first 10 min of irradiation). This indicates that the enhanced amount of toluene degradation by-products generated under visible irradiation can lead to sur-

face blocking and, ultimately, causes a decrease in the efficiency of toluene degradation. A similar effect was observed in our previous work [36]. Additionally, the obtained RE^{3+}-NTs displayed a photostability for the toluene degradation reaction in subsequent cycles. The toluene degradation efficiency remained level at approximately 27% after 60 min of visible light irradiation and four cycles in the presence of the Ho-NTs (Fig. 5b). To confirm toluene mineralization, observation of CO_2 formation during the irradiation of toluene in the presence of Ho-NTs was performed. The CO_2 concentration was monitored using a GC technique with a TCD detector (results are not shown). It was found that the CO_2 concentration increased after 60 min of irradiation, which suggests toluene mineralization.

The most photoactive sample (Ho-NTs) was chosen for performing photocatalytic tests in the water phase under visible light irradiation ($\lambda > 420$ nm), as shown in Fig. 5c. Phenol was selected as a model aqueous phase pollutant. It was found that holmium-TiO_2 NTs showed a 6 times higher photocatalytic efficiency of phenol degradation (16%) than that of the pristine one. The gas and liquid state photocatalysis cannot be properly compared in terms of% efficiency because of several problems e.g., inherent inefficiencies introduced by light absorption or scattering in the aqueous medium [54]. Moreover, these two photocatalytic tests differ in few aspects, such as: (i) irradiation source and light flux (0.25 and $4 \, mW/cm^2$ for gas and aqueous phase, respectively); (ii) volume of irradiated sample ($V_{gas} = 35$ mL; $V_{aqueos} = 25$ mL); (iii) initial concentration of model pollutant ($C_{toluene} = 200$ ppm: $C_{phenol} = 20$ ppm); (iv) presence (aqueous phase) or absence (gas phase) of aeration. Ampelli et al. [53] found that the production of H_2 from ethanol was higher in the gas phase than in the water phase. They concluded that gas phase operations allow better H_2 productivity than liquid phase
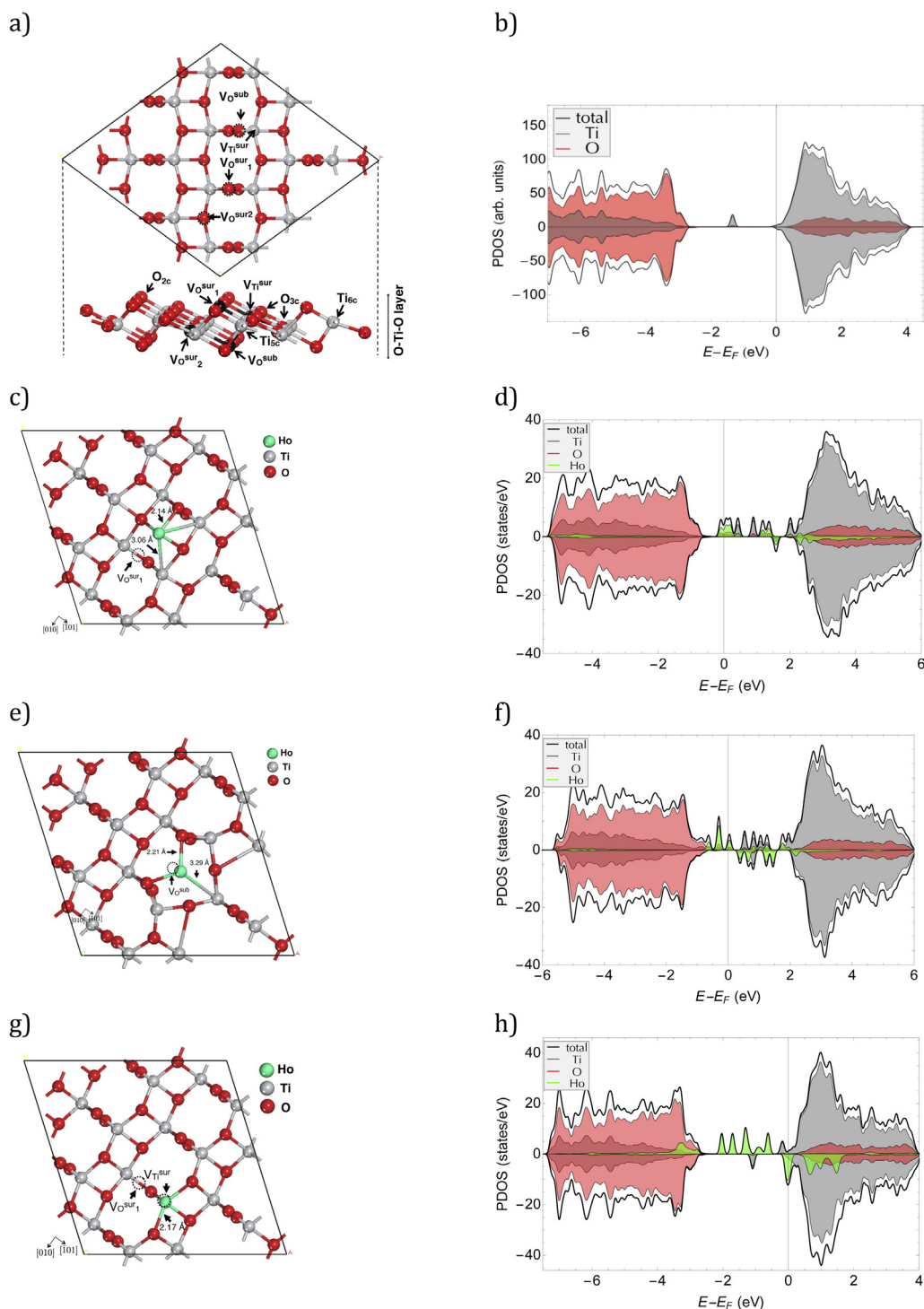
Fig. 6. (a) Side view of the O-Ti-O one-layer TiO$_2$ anatase (101) slab with the possible oxygen vacancy sites on the surface (V$_O^{sur}$) and sub-surface (V$_O^{sub}$); (b) Spin-polarized PBE + U computed PDOS for anatase TiO$_2$(101) with oxygen vacancies. The systems were modelled using a c(4 × 2) lattice; the position of the oxygen vacancies with respect to the most stable Ho-TiO$_2$ structures with (c) V$_O^{sur}$$_1$, (e) V$_O^{sub}$, and (g) V$_{Ti}^{sur}$ (the surface vacancy sites are represented by dotted circles); the spin-polarized PBE + U-computed PDOS for Ho- anatase TiO$_2$(101) with (d) V$_O^{sur}$$_1$, (f) V$_O^{sub}$ and (h) V$_{Ti}^{sur}$ vacancies. The grey, red and green/blue spheres/lines represent Ti, O and Ho, respectively. (For interpretation of the references to colour in this figure legend, the reader is referred to the web version of this article.)

operations because of reduced light scattering. It can be concluded that the photocatalytic reaction in the gas phase requires a lower level intensity of irradiation to perform the reaction and possesses a higher quantum yield of photocatalytic reaction in comparison with the water phase [54,55].

4. Mechanism discussion

The results of the photocatalytic test experiments showed that toluene and phenol can be photodegraded in the presence of RE-NT photocatalysts under visible light irradiation. To understand what type of oxygen species are responsible for the photocatalytic

activity of photocatalysts, a test with the use of terephthalic acid (TPA) was performed. TPA can produce fluorescence compounds when reacted with •OH radicals, and the intensity of the fluorescence peak (PL) of 2-hydroxyterephtalic acid is proportional to the amount of •OH radicals produced in water [2]. Fig. 5d shows the PL intensity change observed after 60 min of irradiation of Ho-NTs under visible light ($\lambda > 420$ nm). As can be seen in Fig. 5d, pristine NTs and RE-NTs exhibit nearly the same PL intensity, and this intensity is very low compared with the literature data [2]. This suggests that RE-TiO_2 modification does not lead to an increase in the production of •OH radicals under visible light irradiation. The obtained results show that other superoxide radicals, for example, $O_2^{•-}$ and •OOH, are responsible for the photodegradation process under visible light irradiation. The formation of $O_2^{•-}$ is probably caused by the reaction of electrons in the conduction band of TiO_2 [56]. To understand the role of the generated electrons in the photocatalytic process, an experiment was conducted in the presence of Cu^{2+} scavengers ($Cu^{2+} + e^- \rightarrow Cu^+$ [57]). We observed no phenol degradation in the presence of Cu^{2+} (Fig. 5d insert graph). This confirms the crucial role of $O_2^{•-}$ in the photodegradation process.

Because our experiments are not conclusive from the perspective of the interaction between RE ion and the TiO_2 lattice, we performed theoretical simulations to understand this interaction. The band structure and partial density of states (PDOS) of pristine and Ho-TiO_2 on the aforementioned geometric configurations are displayed in Fig. 6a–f. From the computed PBE + U electronic structure for $TiO_2(101)$ (Fig. 6b), it can be observed that the surface is semiconducting with a band gap of $\sim$2 eV. The upper valence band (UVB) is dominated by O-2p states, with a small contribution from Ti-3d states. The lower conduction band (LCB) is mainly of Ti-3d character, where the peak at 3 eV is due to Ti-$d_z{}^2$. Analysis of the computed electronic structure of the TiO_2 configurations with the surface vacancy obtained in our previously study indicated that the system of anatase $TiO_2(101)$ with V_O^{sur1} and V_O^{sub} vacancies has a semiconductor ground state, with Ti-3d$_{yz}$ states populating the band gap region of defective anatase $TiO_2(101)$ at $\sim$−1.6 eV and 2 eV, respectively (Fig. 6b) [35]. The defects in the anatase $TiO_2(101)$ surface and the location of the Ho ions in Ho-TiO_2 systems induce the changes in the electronic structure of $TiO_2(101)$. The system (Fig. 6c, e, g) has a semiconductor ground state with Ho-f states populating the band gap of defective anatase $TiO_2(101)$ (see Fig. 6 d, f, h). Moreover, we investigated the geometrical and electronic properties of pristine and Ho-anatase $TiO_2(101)$ with surface vacancies by means of spin-polarized DFT calculations based on the plane-wave pseudopotential method. DFT calculations showed that the formation of V_O^{sur} (Fig. 6c), V_O^{sub} (Fig. 6e) and V_{Ti}^{sur} (Fig. 6g) defects at the surface of Ho-anatase $TiO_2(101)$ results in increased system stabilization, with the total energy (E_{tot}) changing from −290.55 eV for pristine TiO_2 to −1142.71 eV, −1157.82 eV and −1164.71 eV for the TiO_2 structures with V_O^{sub}, V_O^{sur1}, and V_{Ti}^{sur} vacancies, respectively. The synergistic effects of new Ho-f states and surface vacancies may further reduce the photon excitation energy from the VB to the CB under visible-light irradiation, which leads to an enhancement of the visible photocatalytic activity.

Thus, it could be concluded, that the electrochemical oxidation of Ti foil in the first step followed by holmium introduction into the TiO_2 NTs in the second step by using a cathodic electrochemical process, allows to formation of oriented NT arrays modified with Ho and other lanthanides (Er, Yb, Tb, Gd, Pr) Interaction of Ho ions and TiO_2 structure resulted into appearance of new Ho-f states below the conduction band of TiO_2. The proposed photocatalytic mechanism of the RE-NTs excitation under visible light is presented in Fig. 7. In presence of visible light irradiation, the new energy levels can accept electrons from the valence band. Owing to the less energy separation between the new energy levels and the valence band, visible light becomes energetic enough to facili-
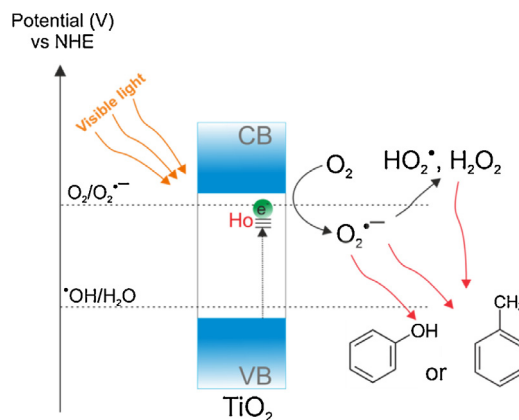

Fig. 7. Proposed photocatalytic mechanism over RE-NTs under visible light.

tate the abovementioned electron transitions. Moreover, based on the photodegradation tests carried out in the presence of Cu^{2+} acting as electron scavenger and terephthalic acid degradation test, it could be stated that $O_2^{•-}$, H_2O_2 and •OOH are responsible for the photodegradation process under visible light irradiation.

5. Conclusions

In summary, highly visible light active NTs modified with Er, Yb, Ho, Tb, Gd, and Pr ions were synthesized via an electrochemical method. From XPS, XRD and KM function analyses, we observed that RE^{3+} species are located at the crystal boundaries rather than inside TiO_2 unit cell and it is very probable that the surrounding rare earth ions formed Ti—O—RE element bonds at the crystal boundary of TiO_2. Excitation into TiO_2 absorption band with resulting RE^{3+} emission confirm energy migration between TiO_2 matrix and RE^{3+}. Moreover, based on the performed calculations, it is proposed that during the electrochemical process, new Ho-f states and surface vacancies are formed and may further reduce the photon excitation energy from the VB to the CB under visible-light irradiation. The photocatalytic activity under Vis irradiation is attributed not to •OH but to other forms of reactive oxygen species ($O_2^{•-}$, $HO_2^•$, H_2O_2).

References

[1] E. Kowalska, M. Janczarek, L. Rosa, S. Juodkazis, B. Ohtani, Mono- and bi-metallic plasmonic photocatalysts for degradation of organic compounds under UV and visible light irradiation, Catal. Today 230 (2014) 131–137.
[2] M. Klein, J. Nadolna, A. Gołąbiewska, P. Mazierski, T. Klimczuk, H. Remita, A. Zaleska-Medynska, The effect of metal cluster deposition route on structure and photocatalytic activity of mono- and bimetallic nanoparticles supported on TiO2 by radiolytic method, Appl. Surf. Sci. 378 (2016) 37–48.
[3] M.S. Hamdy, W.H. Saputera, E.J. Groenen, G. Mul, A novel TiO2 composite for photocatalytic wastewater treatment, J. Catal. 310 (2014) 75–83.
[4] M. Kralova, P. Dzik, M. Vesely, J. Cihlar, Preparation and characterization of doped titanium dioxide printed layers, Catal. Today 230 (2014) 188–196.
[5] J. Wu, S. Lu, D. Ge, L. Zhang, W. Chen, H. Gu, Photocatalytic properties of Pd/TiO2 nanosheets for hydrogen evolution from water splitting, RSC Adv. 6 (2016) 67502–67508.
[6] H. Alarcón, G. Boschloo, P. Mendoza, J.L. Solis, A. Hagfeldt, Dye-sensitized solar cells based on nanocrystalline TiO2 films surface treated with Al3+ ions:

photovoltage and electron transport studies, J. Phys. Chem. B 109 (2005) 18483–18490.

[7] C. Jørgensen, R. Reisfeld, Chemistry and spectroscopy of rare earths, New Trends Chem. 100 (1982) 127–167.

[8] D. Fattakhova-Rohlfing, A. Zaleska, T. Bein, Three-dimensional titanium dioxide nanomaterials, Chem. Rev. 114 (2014) 9487–9558.

[9] C. Wang, Z. Huang, Controlled synthesis of α-Fe2O3 nanostructures for efficient photocatalysis, Mater. Lett. 164 (2016) 194–197.

[10] H. Zhang, H. Ming, S. Lian, H. Huang, H. Li, L. Zhang, Y. Liu, Z. Kang, S.-T. Lee, Fe2O3/carbon quantum dots complex photocatalysts and their enhanced photocatalytic activity under visible light, Dalton Trans. 40 (2011) 10822–10825.

[11] R. Jaiswal, N. Patel, D.C. Kothari, A. Miotello, Improved visible light photocatalytic activity of TiO2 co-doped with Vanadium and Nitrogen, Appl. Catal. B: Environ. 126 (2012) 47–54.

[12] C.-H. Liang, M.-F. Hou, S.-G. Zhou, F.-B. Li, C.-S. Liu, T.-X. Liu, Y.-X. Gao, X.-G. Wang, J.-L. Lü, The effect of erbium on the adsorption and photodegradation of orange I in aqueous Er3+-TiO2 suspension, J. Hazard. Mater. 138 (2006) 471–478.

[13] M. Mba, M. D'Acunzo, P. Salice, T. Carofiglio, M. Maggini, S. Caramori, A. Campana, A. Aliprandi, R. Argazzi, S. Carli, C.A. Bignozzi, Sensitization of nanocrystalline TiO2 with multibranched organic dyes and Co(III)/(II) mediators: strategies to improve charge collection efficiency, J. Phys. Chem. C 117 (2013) 19885–19896.

[14] J. Reszczyńska, T. Grzyb, Z. Wei, M. Klein, E. Kowalska, B. Ohtani, A. Zaleska-Medynska, Photocatalytic activity and luminescence properties of RE3+-TiO2 nanocrystals prepared by sol-gel and hydrothermal methods, Appl. Catal. B: Environ. 181 (2016) 825–837.

[15] J. Wang, Y. Xie, Z.H. Zhang, J. Li, C. Li, L. Zhang, Z. Xing, R. Xu, X. Zhang, Photocatalytic degradation of organic dyes by Er3+:YAlO3/TiO2 composite under solar light, Environ. Chem. Lett. 8 (2008) 87–93.

[16] J. Reszczyńska, T. Grzyb, J.W. Sobczak, W. Lisowski, M. Gazda, B. Ohtani, A. Zaleska, Visible light activity of rare earth metal doped (Er3+, Yb3+ or Er3+/Yb3 +) titania photocatalysts, Appl. Catal. B: Environ. 163 (2015) 40–49.

[17] J. Reszczyńska, T. Grzyb, J.W. Sobczak, W. Lisowski, M. Gazda, B. Ohtani, A. Zaleska, Lanthanide co-doped TiO2: the effect of metal type and amount on surface properties and photocatalytic activity, Appl. Surf. Sci. 307 (2014) 333–345.

[18] H. Cai, G. Liu, W. Lü, X. Li, L. Yu, D. Li, Effect of Ho-doping on photocatalytic activity of nanosized TiO2 catalyst, J. Rare Earths 26 (2008) 71–75.

[19] J.-W. Shi, J.-t. Zheng, P. Wu, Preparation, characterization and photocatalytic activities of holmium-doped titanium dioxide nanoparticles, J. Hazard. Mater. 161 (2009) 416–422.

[20] J. Reszczynska, D. Arenas Esteban, M. Gazda, A. Zaleska, Pr-doped TiO2—the effect of metal content on photocatalytic activity, Physicochem. Probl. Miner. Process. 50 (2014) 515–525.

[21] D. Falcomer, M. Daldosso, C. Cannas, A. Musinu, B. Lasio, S. Enzo, A. Speghini, M. Bettinelli, A one-step solvothermal route for the synthesis of nanocrystalline anatase TiO2 doped with lanthanide ions, J. Solid State Chem. 179 (2006) 2452–2457.

[22] T. Ji, Y. Liu, H. Zhao, H. Du, J. Sun, G. Ge, Preparation and up-conversion fluorescence of rare earth (Er3+ or Yb3+/Er3 +)-doped TiO2 nanobelts, J. Solid State Chem. 183 (2010) 584–589.

[23] M. Nischk, P. Mazierski, M. Gazda, A. Zaleska, Ordered TiO2 nanotubes: the effect of preparation parameters on the photocatalytic activity in air purification process, Appl. Catal. B: Environ. 144 (2014) 674–685.

[24] Y. Li, Y. Wang, J. Kong, J. Wang, Synthesis and photocatalytic activity of TiO2 nanotubes co-doped by erbium ions, Appl. Surf. Sci. 328 (2015) 115–119.

[25] J. Nie, Y. Mo, B. Zheng, H. Yuan, D. Xiao, Electrochemical fabrication of lanthanum-doped TiO2 nanotube array electrode and investigation of its photoelectrochemical capability, Electrochim. Acta 90 (2013) 589–596.

[26] X. Fan, J. Wan, E. Liu, L. Sun, Y. Hu, H. Li, X. Hu, J. Fan, High-efficiency photoelectrocatalytic hydrogen generation enabled by Ag deposited and Ce doped TiO2 nanotube arrays, Ceram. Int. 41 (2015) 5107–5116.

[27] G.A.H. Kresse, J. Hafner, Ab initio molecular dynamics for liquid metals, Phys. Rev. B 47 (1993) R558.

[28] G.H. Kresse, J. Hafner, Ab initio molecular-dynamics simulation of the liquid-metal-amorphous-semiconductor transition in germanium, Phys. Rev. B 49 (1994) 14251.

[29] G.F.l. Kresse, J. Furthmüller, Efficiency of ab-initio total energy calculations for metals and semiconductors using a plane-wave basis set, Comput. Mater. Sci. 6 (1996) 15–50.

[30] G. Mattioli, F. Filippone, P. Alippi, A. Amore Bonapasta, Ab initio study of the electronic states induced by oxygen vacancies in rutile and anatase TiO2Ab initio study of the electronic states induced by oxygen vacancies in rutile and anatase TiO2, Phys. Rev. B 78 (2008) 241201.

[31] G. Kresse, D. Joubert, From ultrasoft pseudopotentials to the projector augmented-wave method, Phys. Rev. B 59 (1999) 1758–1775.

[32] J.P. Perdew, K. Burke, M. Ernzerhof, Generalized gradient approximation made simple, Phys. Rev. Lett. 77 (1996) 3865–3868.

[33] X. Chen, S.S. Mao, Titanium dioxide nanomaterials: synthesis, properties, modifications, and applications, Chem. Rev. 107 (2007) 2891–2959.

[34] E. Finazzi, C. Di Valentin, G. Pacchioni, A. Selloni, Excess electron states in reduced bulk anatase TiO2: Comparison of standard GGA GGA + U, and hybrid DFT calculations, J. Chem. Phys. 129 (2008) 154113.

[35] A. Mikolajczyk, H.P. Pinto, A. Gajewicz, T. Puzyn, J. Leszczynsk, *Ab initio* studies of anatase TiO2 (101) surface-supported Au8 clusters, Curr. Top. Med. Chem. 15 (2015) 1859–1867.

[36] P. Mazierski, M. Nischk, M. Gołkowska, W. Lisowski, M. Gazda, M. Winiarski, T. Klimczuk, A. Zaleska-Medynska, Photocatalytic activity of nitrogen doped TiO2 nanotubes prepared by anodic oxidation: the effect of applied voltage, anodization time and amount of nitrogen dopant, Appl. Catal. B: Environ. 196 (2016) 77–88.

[37] X. Zhou, H. Yang, C. Wang, X. Mao, Y. Wang, Y. Yang, G. Liu, Visible light induced photocatalytic degradation of rhodamine B on one-dimensional iron oxide particles, J. Phys. Chem. C 114 (2010) 17051–17061.

[38] H. Zhang, Y. Sheng, Y. Song, H. Li, J. Huang, K. Zheng, Q. Huo, X. Xu, H. Zou, Uniform hollow TiO2:Sm3+ spheres: solvothermal synthesis and luminescence properties, Powder Technol. 239 (2013) 403–408.

[39] J. Rodríguez-Carvajal, Recent advances in magnetic structure determination by neutron powder diffraction, Physica B 192 (1993) 55–69.

[40] P. Yan, H. Jiang, S. Zang, J. Li, Q. Wang, Sol-solvothermal preparation and characterization of (Yb, N)-codoped anatase-TiO2 nano-photocatalyst with high visible light activity, Mater. Chem. Phys. 139 (2013) 1014–1022.

[41] Y. Ma, J. Zhang, B. Tian, F. Chen, L. Wang, Synthesis and characterization of thermally stable Sm,N co-doped TiO2 with highly visible light activity, J. Hazard. Mater. 182 (2010) 386–393.

[42] Y.A. Teterin, A.Y. Teterin, Structure of X-ray photoelectron spectra of lanthanide compounds, Russ. Chem. Rev. 71 (2002) 347–381.

[43] A.V. Naumkin, A. Kraut-Vass, S. Gaarenstroom, C. Powell, NIST X-ray Photoelectron Spectroscopy Database 20. Version 4.1, 2012.

[44] C. Lazar, E. Burzo, M. Neumann, XPS stupy of RNi4 B compounds, where r = Nd, Tb, Dy, Ho nad Er, J. Optoelectr. Adv. Matter. (2008) 780–782.

[45] T.-M. Pan, L.-C. Yen, X.-C. Wu, A comperative study on the structural properties and electrical characteristics of thin HoTixOy, TmTixOy and YbTixOy dielectrics, Semicond. Sci. Technol. (2010) 055015.

[46] X. Liu, P. Fang, Y. Liu, Z. Liu, D. Lu, Y. Gao, F. Chen, D. Wang, Y. Dai, Effect of holmium doping on the structure and photocatalytic behavior of TiO2-based nanosheets, J. Mater. Sci. 49 (2014) 8063–8073.

[47] H. Ogasawara, A. Kotani, R. Potze, G.A. Sawatzky, B.T. Thole, Praseodymium 3d- and 4d-core photoemission spectra of Pr2O3, Phys. Rev. B (1991) 5465–5469.

[48] S. Jeon, H. Hwang, Electrochemical and physical characteristics of PrTixOy for metal-oxide-semiconductor gate dielectric applications, Appl. Phys. Lett. (2002) 4856–4858.

[49] H.X. Dai, C.F. Ng, C.T. Au, SrCl2-promoted REOx (RE = Ce, Pr, Tb) catalysts for the selective oxidation of ethane: a study on performance and defect structures for ethene formation, J. Catal. 199 (2001) 177–192.

[50] P. Mazierski, J. Nadolna, W. Lisowski, M.J. Winiarski, M. Gazda, M. Nischk, T. Klimczuk, A. Zaleska-Medynska, Effect of irradiation intensity and initial pollutant concentration on gas phase photocatalytic activity of TiO2 nanotube arrays, Catal. Today (2016) http://dx.doi.org/10.1016/j.cattod.2016.09.004.

[51] N.u. Saqib, R. Adnan, I. Shah, A mini-review on rare earth metal-doped TiO2 for photocatalytic remediation of wastewater, Environ. Sci. Pollut. Res. 23 (2016) 15941–15951.

[52] S. Lis, Luminescence spectroscopy of lanthanide(III) ions in solution, J. Alloys Compd. 341 (2002) 45–50.

[53] T. Grzyb, M. Runowski, A. Szczeszak, S. Lis, Influence of matrix on the luminescent and structural properties of glycerine-capped, Tb3+-Doped fluoride nanocrystals, J. Phys. Chem. C 116 (2012) 17188–17196.

[54] P. Mazierski, B. Bajorowicz, E. Grabowska, A. Zaleska-Medynska, Photoreactor design aspects and modeling of light, in: C.J. Colmenares, Y.-J. Xu (Eds.), Heterogeneous Photocatalysis: From Fundamentals to Green Applications, Springer Berlin Heidelberg, Berlin, Heidelberg, 2016, pp. 211–248.

[55] A. Fujishima, T.N. Rao, D.A. Tryk, Titanium dioxide photocatalysis, J. Photochem. Photobiol. C: Photochem. Rev. 1 (2000) 1–21.

[56] S. Ghosh, N.A. Kouamé, L. Ramos, S. Remita, A. Dazzi, A. Deniset-Besseau, P. Beaunier, F. Goubard, P.-H. Aubert, H. Remita, Conducting polymer nanostructures for photocatalysis under visible light, Nat. Mater. 14 (2015) 505–511.

[57] S. Ghosh, A. Priyam, S. Bhattacharya, A. Saha, Mechanistic aspects of quantum dot based probing of Cu (II) ions: role of dendrimer in sensor efficiency, J. Fluoresc. 19 (2009) 723–731.